ISSN 1063-7710, Acoustical Physics, 2021, Vol. 67, No. 6, pp. 619–630. © Pleiades Publishing, Ltd., 2021.
Russian Text © The Author(s), 2021, published in Akusticheskii Zhurnal, 2021, Vol. 67, No. 6, pp. 626–638.

OCEAN ACOUSTICS.
HYDROACOUSTICS

Local Anomalous Sound Field Zones in Shallow Water: Experiment and Simulation

G. N. Kuznetsov[a, *], **I. V. Semenova**[b], **and A. N. Stepanov**[a, b]
[a] *Prokhorov General Physics Institute of the Russian Academy of Sciences, Moscow, 119991 Russia*
[b] *Samara National Research University, Samara, 443086 Russia*
**e-mail: skbmortex@mail.ru*

Received March 10, 2021; revised June 18, 2021; accepted August 3, 2021

Abstract—The paper studies experimentally and theoretically the interference structure of the low-frequency spatial amplitude and phase responses of the scalar field and three projections of the vibrational velocity vector formed by tone signals from towed omnidirectional acoustic sources in zones near the interference maxima and minima of the sound pressure. The experimental dependences of these field characteristics on the distance obtained by four-component vector-scalar receivers when the sources are towed are compared with the calculated ones within the Pekeris model and waveguide model with a three-layer seafloor, the parameters of which were calculated based on acoustic calibration of the operations area. Satisfactory agreement was established between the amplitude and phase responses of the field, calculated by acoustic calibration and measured experimentally. It is shown that in the zones of maxima, a slow change in the angle of arrival is observed and the phase gradients are "smooth", while in the zones of the minimum, sharp jumps in the amplitudes and phases form in the horizontal and vertical planes, leading for deep minima to the formation of circulations: local vortices around the poles. Numerical analysis of the fine structure of the sound pressure and vibrational velocity projections in the acoustic vortex zone is carried out, and hodographs of the vibrational velocity and phase gradients of the sound pressure are calculated, confirming the formation of vortices in the vertical plane in the zone of the poles.

Keywords: shallow water, interference, vector-scalar receivers, phase gradients in the horizontal and vertical planes, signal arrival angles, poles, saddles, acoustic vortices, hodographs, calculations and experiment

DOI: 10.1134/S106377102106004X

1. INTRODUCTION

The use of vector-scalar receivers and arrays makes it possible to reveal the fine three-dimensional amplitude–phase structure of sound fields and study the sound pressures and energy fluxes in the zones of interference maxima (IMA) and in the vicinity of singularities at which the sound pressure tends to zero. This possibility is a consequence of the small size of the receiver versus the wavelength and the dimensions of the anomalous zones themselves. Vector-scalar receivers (VSR), via analysis of the spatial-frequency characteristics of the energy flux lines, make it possible to identify points with a phase singularity, in which in the zone of a deep interference minimum (IMI) (in the limit of zero sound pressure amplitude), poles (dislocations) and vorticity form, while in the zone where the phase gradient or jump in the phase difference between the sound pressure (SP) and vibrational velocity vector (VVV) is a multiple of $\pi/2$, the saddle points of the phase front can be found and studied. Some pioneering results of analytical and numerical solution of this problem in shallow water with a cross section of the field in the horizontal plane are presented in [1–3]. In [4], similar patterns were discovered and investigated for a cross section of the field in the vertical plane.

The results of experimental studies and their analysis are given in [3, 5–8]. In particular, these studies note that the sound field properties in IMI zones are sensitive to variations in the waveguide characteristics, e.g., its depth. The study of the interference amplitude and phase structure of the SP and the projections of the VVV for towed low-frequency tone emitters has been carried out. A rather interesting comparison of the phase gradients in the horizontal and vertical planes with the general theoretical concepts of the vector structure of hydroacoustic fields has been done, including analysis of the vortex structure, but only for the free space [6, 7]. Therefore, it is necessary to compare the experimental data with the results of computer simulation of the field in a multimode waveguide. For comparison, we use two models of the waveguide transfer function, constructed for the same operations area by acoustic calibration of the parameters of the seafloor model. Calibration means that, under controlled conditions, by solving the inverse

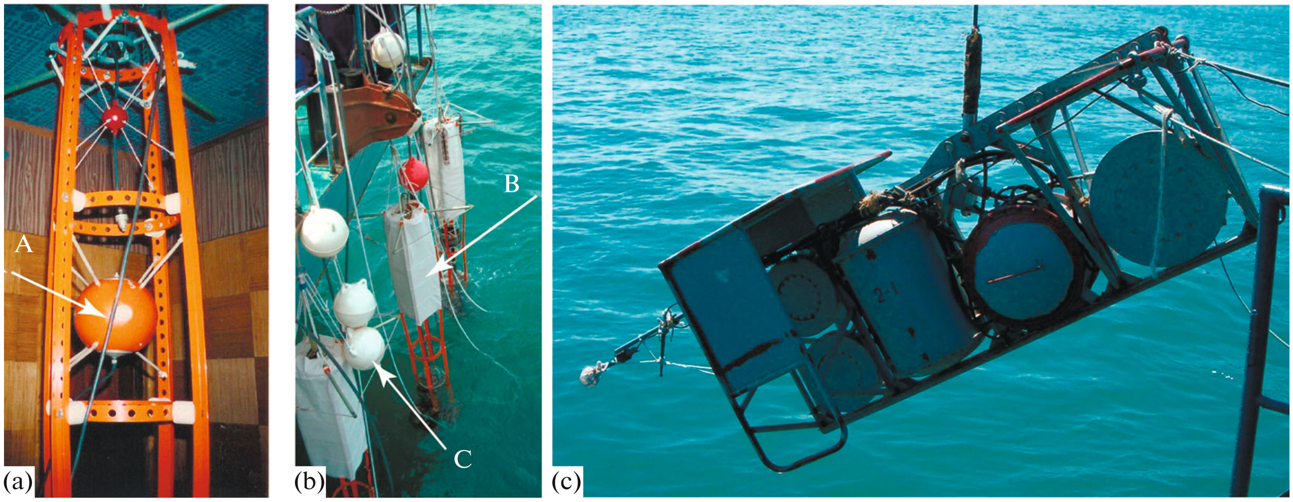

Fig. 1. (a) Frame with low- (10–1200 Hz) and high-frequency VSR (1–10 kHz). (b) Frames with VSR at side of vessel, prepared for mooring; A, low-frequency receiver; B, fairing; C, floats. (c) Towed emitting complex with emitters and equipment.

problem—with a known array geometry and source path, as well as sound velocity profile—the seafloor parameters are selected, but within the accepted waveguide models. The first is the well-known Pekeris model, when a real waveguide is replaced by a homogeneous fluid layer lying on a fluid half-space. The second model is more complex and represents a water layer, two fluid seafloor layers, and an elastic half-space. Further, the seafloor parameters obtained by calibrating a given area are used to construct a model of the waveguide transfer function and calculate the characteristics of interest, which makes it possible to compare the calculated and experimental vector-scalar characteristics of signals. For scalar fields, this problem has been repeatedly and successfully solved, e.g., in [9–11]. The authors are unaware of solutions in this formulation for vector-scalar fields.

Below, to solve the posed problems, the spatial amplitude-phase structure of the vector-scalar field of signals from tone emitters towed in shallow water on rectilinear legs is studied experimentally and numerically. In this case, the results of analyzing the experimental data are compared with the characteristics of the vector-scalar fields calculated using mode models of the waveguide constructed on the basis of the acoustic calibration of the operations area.

A detailed computational and theoretical analysis of the vertical–horizontal structure of the SP field and orthogonal projections of the VVV in a deep IMI zone (a probable dislocation zone) is also carried out. For this zone of the waveguide with the limiting characteristics, the fine structure of the SP and vortex components of the VVV and phase gradient of the SP were studied [5–8]. The idealized interference structure of the SP field with identification of dislocation zones and saddles was calculated, and hodographs of the vibrational velocity and phase gradient of the SP were obtained, confirming the formation of vortices in the zone of poles predicted in [1, 2, 4].

A conclusion is drawn about the feasibility of further research and analysis of the spatial-frequency responses of the field in the IMA zones using VSRs.

2. EXPERIMENTAL CONDITIONS

In the experiments, signals were received by spatially offset low-frequency four-component VSRs, including one scalar and three orthogonal vector inertial receivers (Fig. 1a, position A). VSRs were placed in a frame, around which a sound-transparent fairing was attached, which formed a dead zone (Fig. 1b, position B). The receivers were placed using floats in a position close to vertical on the Z axis (Fig. 1b, position C). The low-frequency VSRs were located at a depth of about 1 m from the bottom. The raised receiver module was moored at a depth of 33 m. The sea depth in the operations area based on echosounder data was 53 m. Note that the receivers were almost spatially immobile and their orientation after mooring was stable, but periodically refined using pulsed acoustic signals with simultaneous estimation of the emitter coordinates via a GPS system. The experiments were carried out with towing of the three emitters at a depth of 24 m, a speed of 1.67 m/s, on the same frame, emitting tone signals at frequencies of 117, 320, and 650 Hz (Fig. 1c). The total aperture of the bottom array was 100 m (Fig. 2a).

The towing depth was chosen under the assumption that the mode structure would be simplified for the probable seafloor properties: the amplitudes of even modes would be minimal. Analysis of the mode structure showed that the seafloor was hard and the wave spectra turned out to be multimodal: 7–9 modes were used to construct the Pekeris model at a fre-

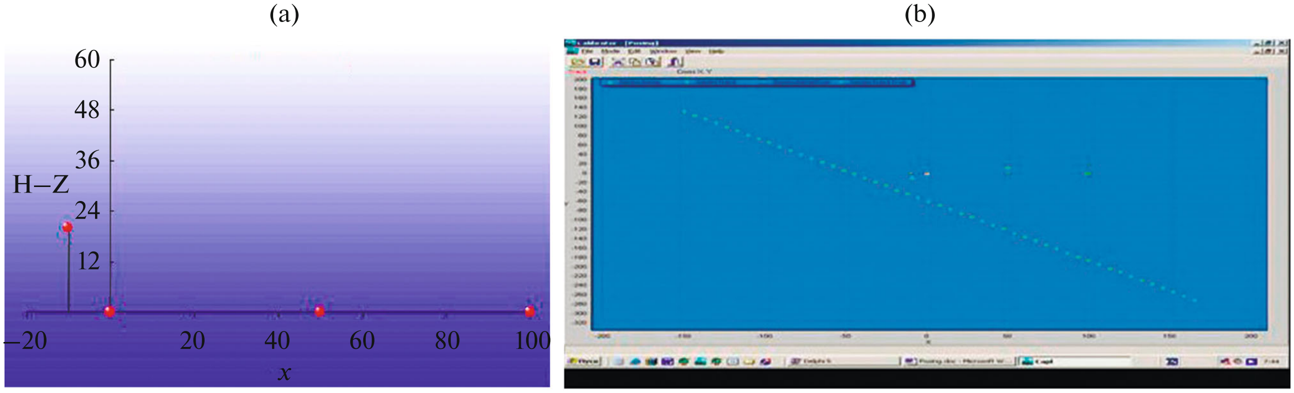

Fig. 2. (a) Diagram of VSR placement in vertical plane and (b) section of emitter towing path with respect to spatially offset receiver modules (four points).

quency of 117 Hz, and up to 11 modes for the three-layer model. At a frequency of 320 Hz, 15–18 modes were formed within the Pekeris model, and up to 24 modes for the three-layer model. Such a large number of even and odd modes leads to relatively smooth decay of the SP amplitudes in the IMA zones and moderate IMI values. Note also that, in each group, modes with numbers greater than three have a small amplitude, and half or more are leaky modes that rapidly decay even at small distances.

The emitters were towed out along rectilinear lines with respect to the receiver modules, the layout of which is shown in Fig. 2a. Figure 2b shows a segment of the emitter towing trajectory closest to the array, recorded in real time as seen in the screenshot The length of the section of the towing trajectory in this figure was ±250 m; the traverse distance to the nearest bottom receiver was 25–30 m. The length of the bottom arrays shown in Fig. 2 was 100 m. The receivers were located to the right of the trajectory. The towing vessel coordinates were recorded by GPS. The total length of the section of the path selected for signal processing was 2000 m. The moment of the traverse is indicated by “0” (Fig. 3). Since before the experiments, not only the waveguide, but also the array were acoustically calibrated, in particular, the geographical coordinates of the receiver elements were calculated, the coordinates of the receiver system, towing vessel, and the emitters can be depicted on one graph. As a consequence, the coordinates of the emitter relative to the receiver modules were calculated. The results of processing sound signals on one of the rectilinear legs are shown below in Fig. 3.

3. ANALYSIS OF THE EXPERIMENTAL RESULTS

For frequencies 117 and 320 Hz, Fig. 3 shows the distance interference dependences of the SP P, vertical Z-component of the VVV, phase difference between the SP and Z-component ($\Delta\varphi_{PV_z}$), integral incursion of the phase difference between the SP and vertical component of the VVV ($\Delta\Phi_{PV_z}$), as well as the angle of arrival in the vertical plane of the equivalent plane wave (angle elevation), obtained synchronously in the universal time system are presented. This angle was calculated using the formula $\theta = \arctan(\langle P^*V_z\rangle/[\langle P^*V_x\rangle^2 + \langle P^*V_y\rangle^2]^{1/2})$, where the asterisk denotes complex conjugation. The results of analyzing the interference of the horizontal projections of the VVV (V_x and V_y) are not given here, since they coincide in detail with the distance dependences of the SP interference curves. This is confirmed by the similarity of the transmission curves (Figs. 3f, 3g), constructed from the horizontal projections. These figures (Fig. 3g) show the distance dependences of the phase difference between the SP and three VVV projections V_x, V_y, and V_z. Clearly, in the horizontal plane, when passing through zones with minimum sensitivity V_x and V_y, 180° phase jumps are observed, as well as sign-alternating phase jumps during passage of sections with deep IMI (distances of 950 and 1520 m). Similar deviations can be seen when analyzing the phase difference between the pressure and vertical projection V_z.

The results for 650 Hz are not given either, since they qualitatively illustrate the same dependences as for lower frequencies. However, with an increase in frequency, owing to an increase in the number of normal waves in the spatial domain, a much rougher structure is formed, which complicates interpretation of the results.

Figures 3a and 3b show that in the near-field zone at distances up to 1.5 sea depths, according to the ray approximation, the distance dependences of the SP and vertical projection of the VVV are similar. After the formation of normal waves, the interference structures of the SP field and horizontal VVV projections differ markedly from the dependences for the VVV projection. These dependences are different, because the vertical vector receiver suppresses modes with the first numbers and emphasizes modes with high num-

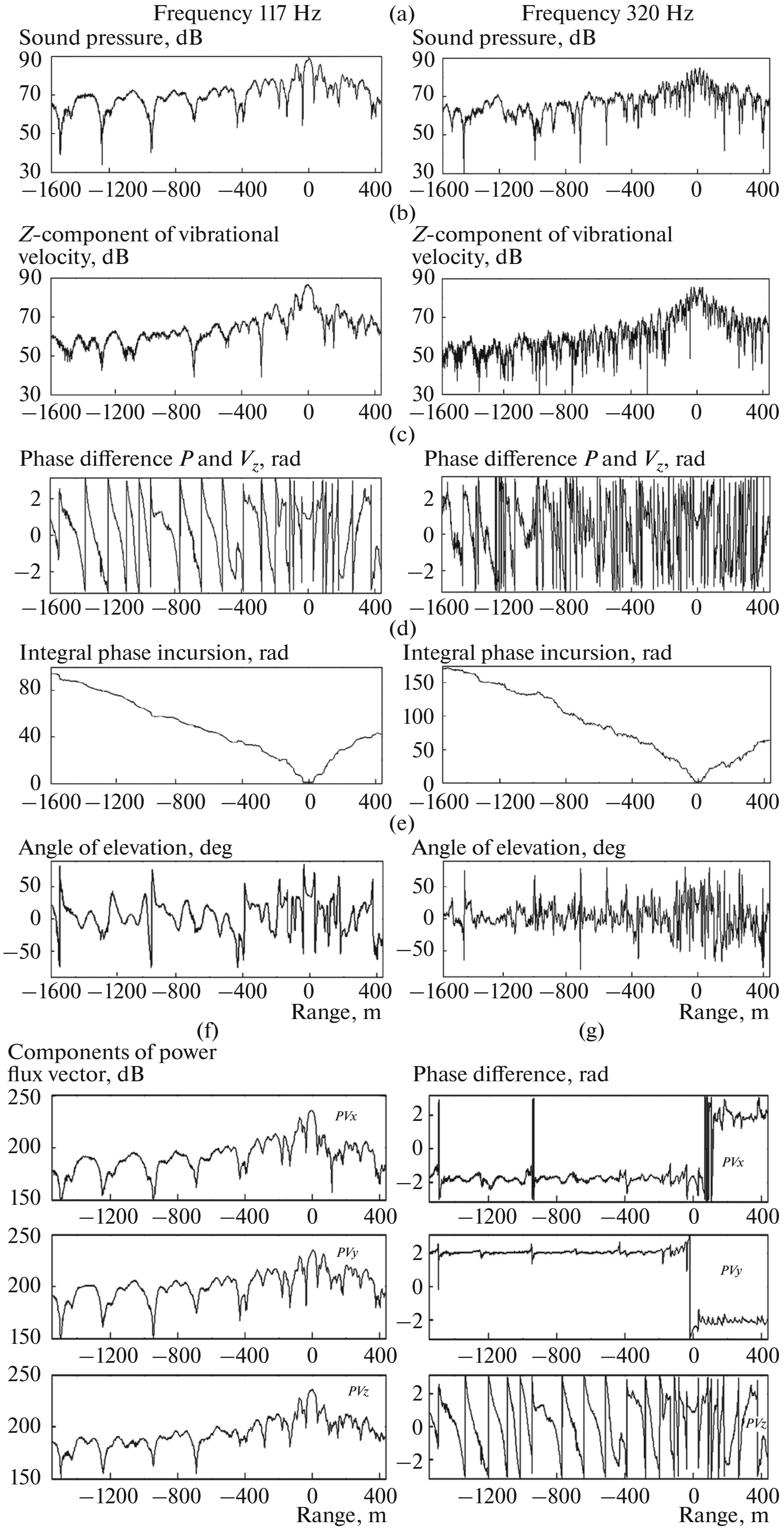

Fig. 3. Experimental data for frequencies of 117 (left) and 320 Hz (right): (a) SP amplitude; (b) Z-component of vibrational velocity; (c) local and (d) integral phase difference between SP and Z-component; (e) angle of elevation of VVV in vertical plane. Distance dependences of SP amplitude and phase difference of three orthogonal components of power flux vector ((f) and (g), respectively; frequency 117 Hz).

bers, while the horizontal receiver does the opposite. Thus, different mode groups are summed at the outputs of these receivers. This leads, in particular, to difference in the length of the IMA zones and relative displacement of the zones of SP minima and the vertical projection of the VVV, as well as zones of phase jumps for these two groups of signals near the IMI zones of the sound pressure. As a consequence, sharp jumps in the phase gradients are observed between the SP and the vertical projection of the VVV. The transmission curves also differ, especially in the IMI zones.

Note also that the amplitudes of the vertical projection of the VVV decrease with increasing distance faster than the SP and horizontal projections of the VVV. For example, at a frequency of 117 Hz at a distance of 1600 m, the SP decreases by 22 dB, and the vertical projection of the VVV, by 28 dB. At 320 Hz, the corresponding values are 19 and 27 dB, respectively. This is because the vertical projection of the VVV is formed by modes with high numbers, which decay faster with increasing distance than modes with the first numbers. This agrees well with the computer simulation results presented in [12, 13].

Analysis of the distance dependences of the local phase differences shows that near the IMI, the phase gradients rapidly increase and become uncertain (unpredictable). Moreover, the deeper the minimum of the dependence $P(r(t))$, the larger the jump in the phase difference. It follows from the theory [1, 2, 4] that, depending on the distance of the horizontal or vertical cross section of the field from dislocations (poles) located at certain depths, unilateral jumps in the phase difference are possible by up to π rad. However, since the cross section at a towing depth of 24 m does not directly intersect the dislocation depth, phase jumps equal to $\pm\pi$ are not observed. It can be seen that at distances of 400, 950, and 1550 m (117 Hz) and 350, 700, and 1450 m (320 Hz), phase jumps in the vertical projection of the VVV lead to varying angles of arrival $\pm(75°–80°)$. However, there are no deep minima, because the field is formed by modes with both even and odd numbers, the spatial periods of interference of which do not coincide. However, with increasing distance and degeneration of high-number modes, the depth of the IMI can increase if the signal is strong and the waveguide regular. In an irregular stochastic waveguide, the modes should lose coherence and the minima will be largely blurred.

It also follows from the theory that for the immediate cross section of the dislocation zone (deep minimum), i.e., during the passage of a "dislocation", there should be a complete turn in the direction of the power flux and a change in phase by 2π [1–4]. At the same time, deviations from the linear dependence of the integral phase $\Delta\Phi_{PV_z}$ when passing around a singularity (dislocation), the phase changes by $+2\pi$ or 2π (Figs. 3c, 3g) depending on the type of poles [1, 2, 4]. In the experiment, phase jumps can only tend to these values, since even in zones in which the quantities P, $|V_x|$, $|V_y|$, $|V_z|$ tend to the minimum value, the IMI depth is insignificant. Nevertheless, there are simultaneous phase jumps in the horizontal and vertical planes, which have different gradients and signs. Therefore, the poles can be fairly close in distance.

Note that in some zones, the phase gradient is continuous and passes through zero when the phase sign changes. Saddles are formed at these points (Figs. 3 and 4).

It is important that the zones with deep IMI separate the zones in which pronounced IMA are formed. In these zones, extended zones form, which are more important for solving practical problems, which have an increased signal-to-noise ratio, smooth phase gradients, a slow variation in the direction of signal arrival in the vertical plane, and, accordingly, slower variation in the angle elevation (see Figs. 3, 4). Therefore, in these zones, for a long time, the sound energy arrives at the receiver point at a constant receiver angle, which allows it to be effectively accumulated to increase the signal-to-noise ratio. When placing the array in IMA zones and taking into account the real distribution of the phase gradients and SP amplitudes on the array aperture, directivity patterns with unbiased bearing estimates are generated [14]. These conclusions are substantiated below. Note once again that in the operations area, acoustic calibration was performed, on the basis of which several seafloor models and waveguide transfer functions were constructed, in particular, in relation to the Pekeris waveguide and waveguide with a three-layer seafloor. Let us show that the use of adequate models makes it possible to obtain satisfactory agreement between the calculated and experimental characteristics not only for the scalar, but also for vector-phase characteristics of the field. The use of mode models, but with other seafloor parameters, does not yield experimental and calculated dependences even approaching each other.

4. RESULTS OF VECTOR-SCALAR FIELD SIMULATION IN A WAVEGUIDE

Let us consider the results of computer simulation of the vector-scalar characteristics of the sound field in a waveguide. The analysis was performed for a waveguide with equivalent seafloor parameters calculated for frequencies of 117 and 320 Hz and seafloor models developed using experimental acoustic calibration [9–11].

Figures 4, 5 show the curves calculated for rectilinear passage of the source past a stationary vector-scalar receiver under the following conditions: depth of the water layer $h = 53$ m, sound speed in water $c_0 =$ 1470 m/s, source depth $z_s = 24$ m, receiver depth $z_r =$ 33 m, length of section of rectilinear leg of source up to traverse 1600 m, length of section after traverse 400 m, and distance of traverse to nearest VSR $r_t = 40$ m. The

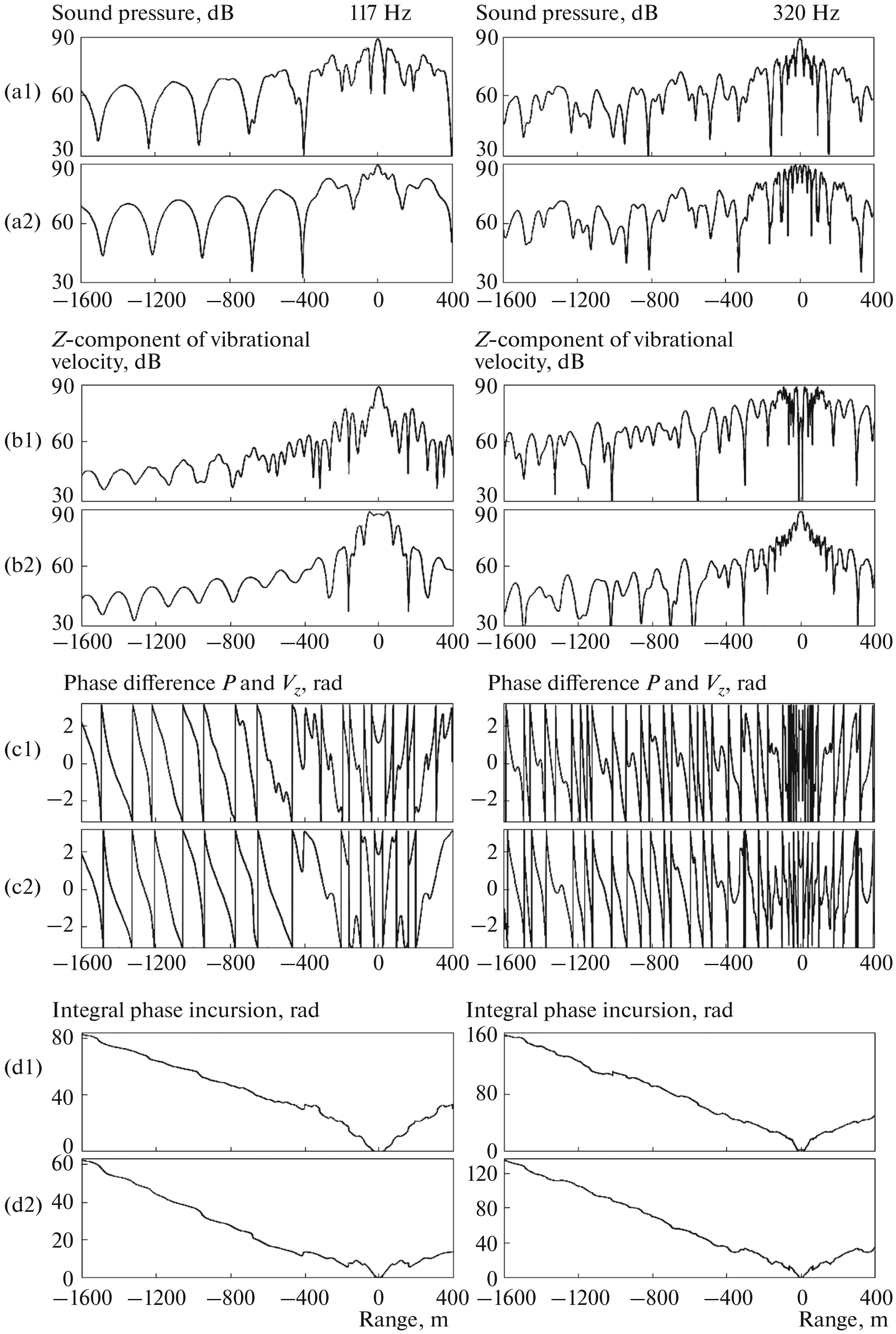

Fig. 4. (a–d) Calculated distance dependence of SP for Pekeris model (a2–d2) and three-layer seafloor model (a1–d1) for frequencies of 117 and 320 Hz; Z-component of vibrational velocity; and (c) local and (d) integral phase difference between SP and Z-component.

horizontal axis is the distance from the moving source to the point of the traverse. The calculations were performed for two models with the following parameters. For the single-layer Pekeris model: $\rho = 1.5$ g/cm^3, $c = 1650$ m/s, $\alpha = \mathrm{Im}\, c/\mathrm{Re}\, c = 0.008$; for the three-layer seafloor model: seafloor layer 1: $\Delta h = 2$ m, $\rho = 1.5$ g/cm^3, $c = 1608$ m/s, $\alpha = \mathrm{Im}\, c/\mathrm{Re}\, c = 0.008$; seafloor layer 2: $\Delta h = 150$ m, $\rho = 2.0$ g/cm^3, $c = 1694$ m/s, $\alpha = 0.008$; homogeneous half-space 3: $\rho = 2.5$ g/cm^3, $c = 2890$ m/s, $\alpha = 0.008$, $c_t = 448$, $\alpha_t = 0.012$. Figure 4, just like Fig. 3, shows for frequencies 117 and 320 Hz (left and right) the distance dependences of the amplitude of the SP (Figs. 4a1, 4a2) and Z- components of the VVV (Figs. 4b1, 4b2), local phase differences of the SP and Z-components of the vibrational velocity ranging from $-\pi$ to $+\pi$ (Figs. 4c1, 4c2), as well as the integral incursion of the phase difference of the SP and Z-component of the vibrational velocity (Figs. 4d1, 4d2). In Fig. 4, graphs 4a2–4d2 correspond to the three-layer seafloor model, and graphs 4a1–4d1, to the Pekeris model.

Figure 5 shows the following for frequencies 117 and 320 Hz: (a) local phase difference arg (PV_x) between P and V_x [rad]; (b) local phase difference arg(PV_y) between P and V_y [rad]; (c) *1*, φ_r' the horizontal and *2*, φ_z' vertical projection of the SP phase gradient; (d) *3*, the effective phase velocity calculated as the weighted average phase velocity of the modes, *4*, the effective phase velocity calculated using the phase gradients in the IMA zones [14, 15], (e) the angle elevation (angle of arrival of an equivalent plane wave) with respect to the horizontal plane (deg); and (f) bearing to the moving source (deg).

From comparison of Figs. 3–5 it follows that the experimental and calculated dependences P and V_z, basically agree well with each other both in the interference curves and local phase gradients, as well as in the largest integral phase incursion and mean laws of decay of amplitudes of the SP and vertical projection of the VVV. The integral phase incursions $\Delta\Phi_{PVz}(r(t))$ and distances at which the moments of intersection of zones with minimum sensitivities V_x and V_y (dipole axes) are recorded virtually coincide. There is agreement between the moments of passage of the traverse distance, at which the phase difference $\Delta\Phi_{PVz}$ is minimal, $\arg|PV_z| \to \min$. The calculated zones of variation in the sign of the bearing to the source and experimental values of these characteristics also coincide. Phase jump zones during passage of depths with minimum V_x and V_y values are close, e.g., rotation of the phase gradient at a distance of 400 m (frequency 117 Hz), but they do not always coincide. The more complex and more adequate three-layer seafloor model is in better agreement with the experimental data than the Pekeris model. This difference is especially noticeable in the traverse zone. This is because in the calculations using the simplified Pekeris model at small distances, the lateral wave was not taken into account, and only the discrete trapped mode model was used [9, 10]. Some difference in the experimental and calculated interference dependences can also be explained by errors in estimating the current distance between the receivers and towed transmitter. This is confirmed by the increase in the indicated difference in the transmission curves when using high versus low signal emission frequencies.

It should be noted, however, that the interference structures of the vertical projection of the VVV calculated using the two models agree much worse with the experimental curves than for the SP. Hence, it follows that during acoustic calibration, high-number modes were estimated with a greater error than modes with the first numbers.

Figure 5 also shows the distance dependences of the bearing for 117 and 320 Hz, as well as the results of calculating the phase gradient in the horizontal and vertical planes. These data is used in the next section for constructing the hodograph of the phase gradients. It can be seen that, at the two frequencies, the estimates of the bearing and zone of passage of the point on the traverse nearly coincide. The phase derivatives in the horizontal plane φ_r' in the IMA zones are quite stable and depend weakly on frequency and distance. This makes it possible to estimate the local phase gradients and effective phase velocity, the use of which is recommended in forming the directivity pattern in the horizontal plane [13–15]. The average derivatives of the phase in the vertical plane φ_z' are close to zero, which seems an important result, since it can be used by vertical receiving or transmitting arrays to form spatial responses.

By comparing the experimental results and simulation data with the general theoretical concepts, it can also be concluded that both in the calculated curves and in experiment, a small number of deep minima are observed, in contrast to data [9], where interference at a low frequency of 48 Hz was determined as odd-mode interference. At higher frequencies in a multimode waveguide, in-phase summation of all normal waves is impossible in principle because of the nonmultiple interference periods of normal waves with even and odd numbers. For example, in [16], it is shown that the spatial scale of the IMA zone for the first and third modes $\Lambda_{1,3} \approx H^2/\lambda$, and for the first and second modes $\Lambda_{1,2} \approx 8H^2/3\lambda$, where $\lambda = 2\pi/k$, k is the horizontal projection of the wavenumber, and H is the equivalent depth of a waveguide with two ideal boundaries [17]. Thus, the IMA zones formed by modes with different numbers are not actually multiples.

Emission frequency 117 Hz

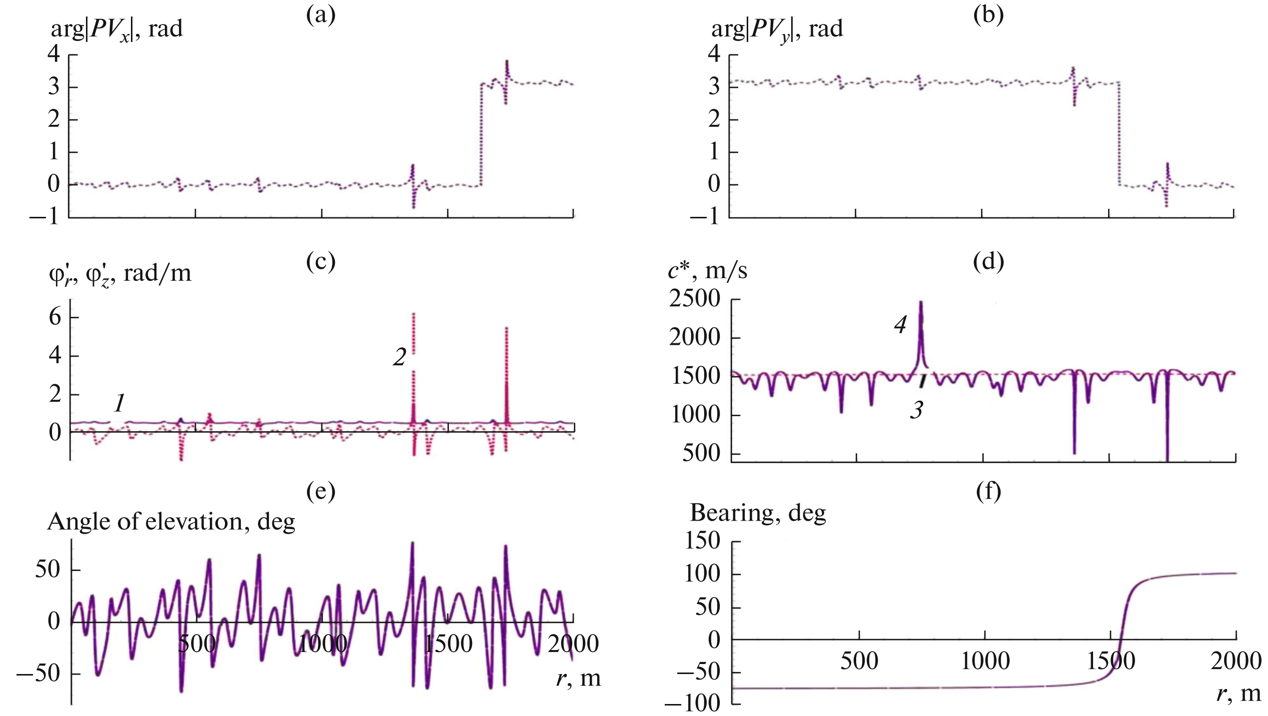

Emission frequency 320 Hz

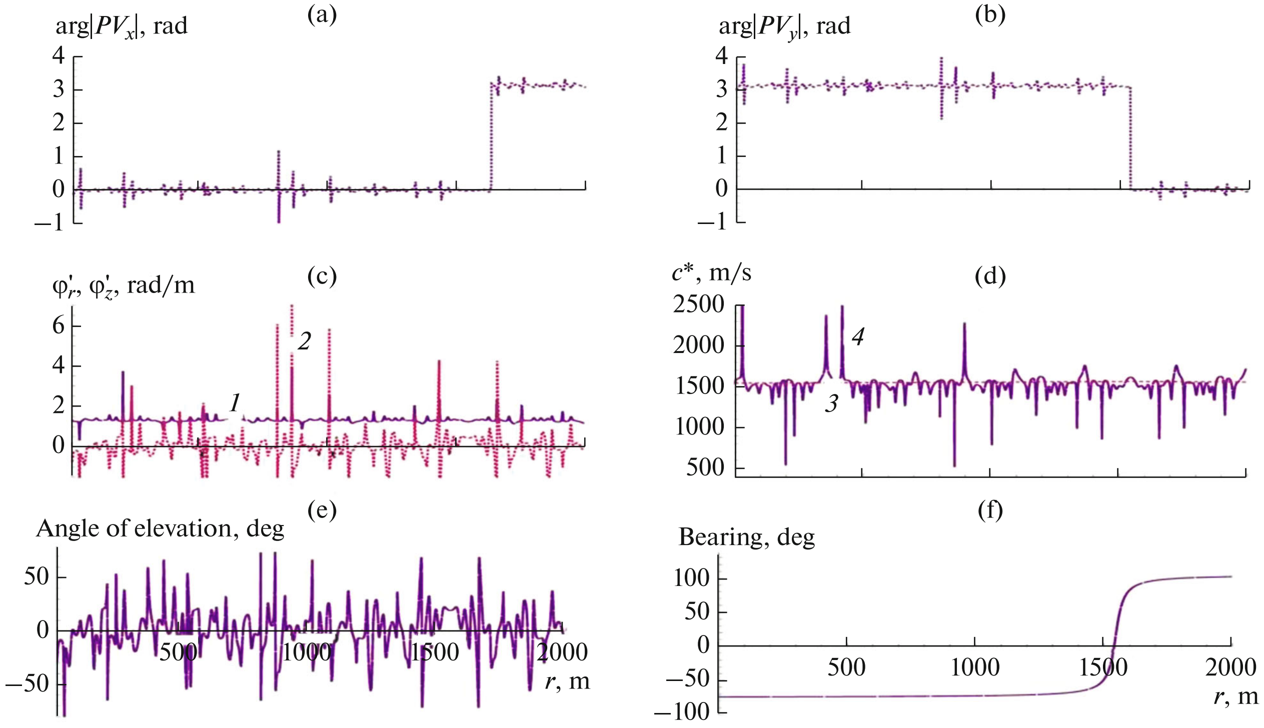

Fig. 5. Calculation results for Pekeris waveguide with equivalent seafloor characteristics: (a, b) local phase difference between SP and horizontal projections of VVV; (c) *1*, horizontal and *2*, vertical projection of SP phase gradient; (d) *3*, effective phase velocity calculated as weighted average phase velocity of modes; *4*, effective phase velocity calculated using phase gradients in IMA zones; (e) angle of elevation with respect to horizontal plane, and (f) bearing to moving source. Top, for 117 Hz; bottom, for 320 Hz.

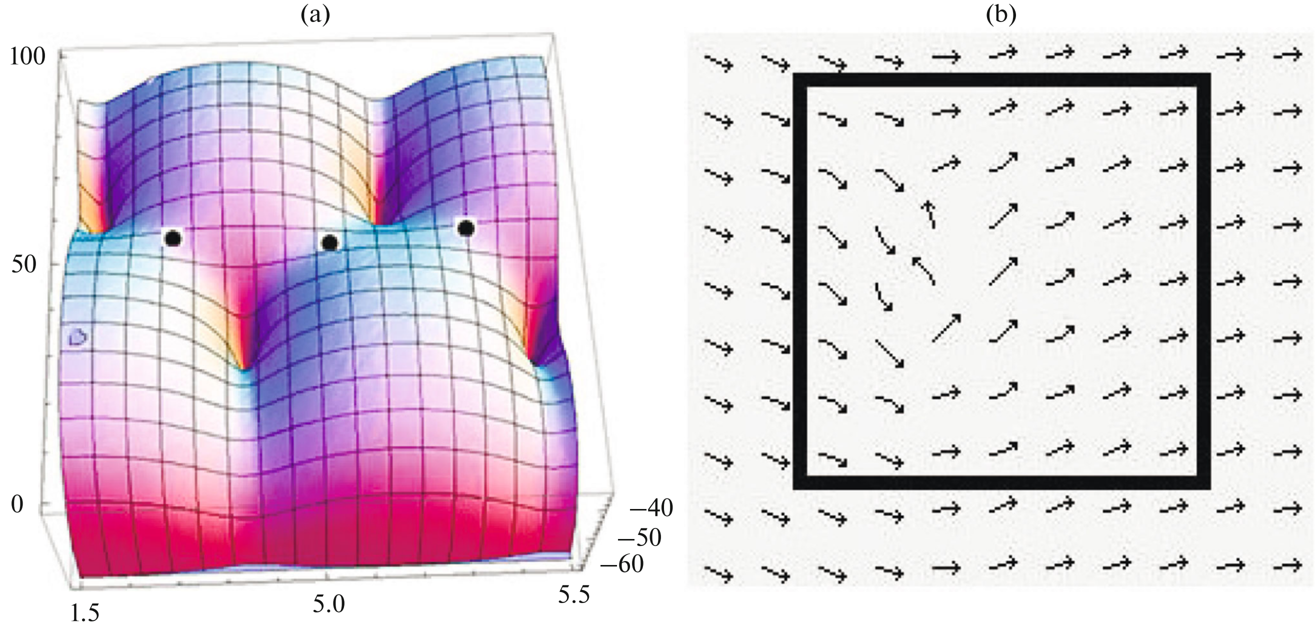

Fig. 6. (a) Distribution of SP amplitude in vertical-horizontal plane as function of depth and distance to source. (b) Distribution in VVV space near dislocation.

5. ANALYSIS OF THE STRUCTURE OF THE FIELD NEAR DISLOCATIONS

Let us first consider enlarged representations of the spatial structure of the SP field with identification of pole and saddle zones (Fig. 6a). The axes in three-dimensional Fig. 6a show the distance from 4.5 to 5.5 km, emitter depth from 0 to 100 m, and AP amplitude [dB]. To simplify analysis of the mode and interference structure, calculations were performed at a low frequency of 25 Hz for a waveguide depth of 100 m, when only two normal waves are formed in the waveguide. The receiver is located on the bottom, and the depth of the emitter varies from surface to bottom, which makes it possible to obtain cross sections of the sound field in the vertical plane at different distances. In the figure, deep dips indicate dislocation zones, and black dots indicate saddles. It can be seen that the dislocations are localized at certain depths, and only at them can deep minima be obtained. The coordinates of these zones depend on the sound frequency and, as a consequence, zones with the minimum SP values are smeared in the frequency-spatial domain. Therefor, the use of vortex patterns for detecting broadband signals, in our opinion, is not possible.

Figure 6b shows the results of calculating the spatially varying directions of the VVV calculated near the lower left dislocation (see Fig. 6a). For this, in the vicinity of this dislocation, an area with dimensions of 10 × 10 m was cut in the vertical plane. One can be see that, far from the dislocation, the oscillating particles of the fluid bend around the dislocation zone, forming a horizontally propagating sound energy flux outside these zones. In the immediate vicinity of the dislocation, vibrational particles change direction by 90° and even 180°; i.e., a sound vortex is formed. These results agree well with the data in Fig. 7, which presents the calculated dependences of the amplitude and the local phase of the SP on depth and distance to the source, as well as the values of the horizontal and vertical projections of the VVV and phase gradient. Figure 7 also shows the vertical cross section of the field from the free surface to the bottom, including IMA and IMI areas. The hodographs of the vibrational velocity vector and the phase gradient vector are calculated. The calculations were performed in a Pekeris waveguide with the following characteristics: thickness 100 m, speed of sound in water c_0 = 1450 m/s, seafloor parameters: the ratio of the densities of seafloor and water $m = 1.8$ and the ratio of the speeds of sound in water and in seafloor $n = 0.725$; absorption coefficient 0.02. To obtain a more relief structure, calculations were performed for a relatively low frequency of 25 Hz. The depth of the receiver is 100 m, the depth of the emitter varies from zero to the depth of the waveguide, the distance to the receiver is 20 km.

Joint analysis of Figs. 3–7 demonstrates the following:

— In the SP IMA zones, the phase gradients in the horizontal plane tend to a constant value, and in the zone of the deep minimum, when the depth of the emitter changes by only a few meters, the phase magnitude changes abruptly by 180° (see Fig. 7, curve *4*). In the vertical plane, the phase gradients in the IMA zone are virtually zero (curve *6*), which makes it possible on vertical arrays to coherently sum signals arriv-

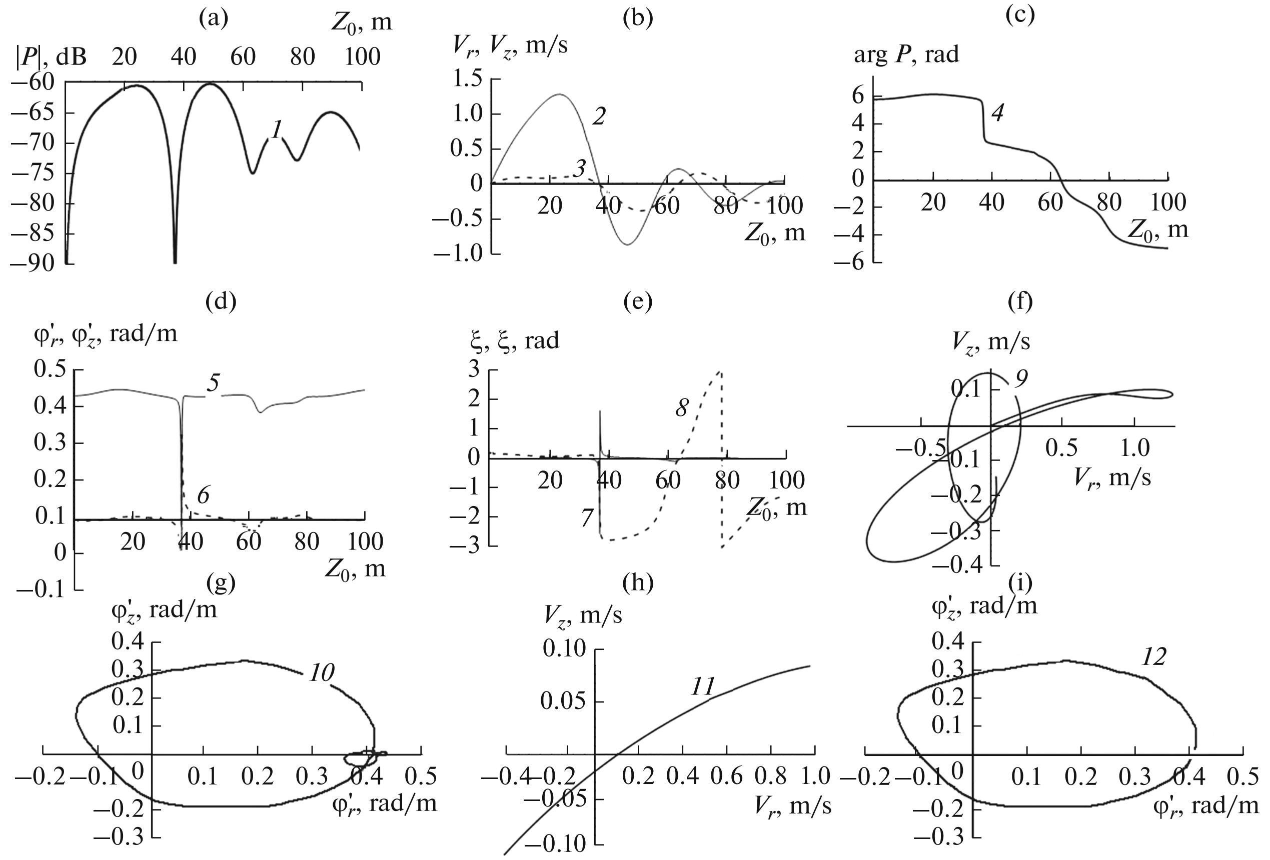

Fig. 7. Depth distributions of amplitude and phase characteristics of SP, projections of VVV and angles of arrival of signals, as well as hodographs of VVV and phase gradient (see text for curve notation).

ing at spatially offset hydrophones within the IMA zone.

— In the IMA zones, the projections of the VVV (curves *2*, *3*) may be in-phase, but they may also be in antiphase, depending on the location of the receiver or emitter with respect to the coordinates of dislocations [1, 2, 4], but in the zone of the deep minimum at an emission depth of 37.2 m (curve *1*), both projections, like the SP, tend to zero. In the IMA zone, the horizontal component of the VVV significantly exceeds the vertical component, and this result is typical of shallow water.

— The phase gradients in the horizontal plane in the deep IMI zone sharply increase and change sign (curve *5*). When passing through the IMI zone, the phase gradient in the vertical plane changes sign twice and sharply increases to values of $\pm\pi$ (curve *6*). Outside of IMI, these gradients are quite stable.

— The angles elevation (direction of arrival in the vertical plane) of the total vector of the phase gradient (curve *7*) and direction (angle of arrival) of the total VVV (curve *8*) are calculated by the formulas ξ = arctan φ_z/φ_r, ζ = arctan V_z/V_r [rad]. Calculations show that in the zone of the first SP maximum, these angles coincide in direction, which indicates the possibility of using an equivalent plane wave model in the zone of the maximum [10, 11] and formation of a power flux in the horizontal plane. In the zone of the second maximum after the deep minimum, the directions of the phase gradient and vibrational velocity vectors are parallel, but oppositely directed. The reason is that vorticity forms around the deep minimum point (pole) and the power flux turns by 180°.

— The hodograph of the VVVs in the IMI zone (curve *9*) also indicates a change in direction of vibrational motion and the formation of an acoustic vortex—circulation of the power flux around the pole (dislocation).

— The hodograph of the phase gradient vector (curve *10*) also confirms this. In Fig. 7, the horizontal derivative φ_r is indicated on the *x* axis; on *y* axis, vertical derivative φ_z. Both phase gradient projections form the total gradient vector.

— Curve *11* shows the hodograph of the VVV, but only in a narrow zone of the deep minimum—in a limited depth interval of the emitter of 30–40 m. The *x* axis is the horizontal component V_r; the *y* axis, the vertical component V_z. The total VVV in the SP IMI zone virtually reaches a zero value.

— The hodograph of the phase gradient vector near the zone of the deep minimum (emitter depth 30–40 m) is shown by curve *12*. The *x* axis is the horizontal component φ_r; the *y* axis, the vertical component φ_z. This confirms the presence of an inverse power flux in the vorticity zone, since the directions of the Umov–Poynting vector and SP phase gradient vector coincide.

— Figure 7 also demonstrates that in the zone of the deep minimum of the SP (curve *1*, the source depth $z_0 = 37/2$ m), the SP, and both projections of the VVV tend to zero (curves *2*, *3*, *11*).

6. CONCLUSIONS

In shallow water, the amplitude-phase responses of a low-frequency vector-scalar sound field in the zones of interference maxima and minima have been studied experimentally and numerically. It was found that analysis of the vector-scalar structure yields an idea of unidirectional acoustic energy fluxes, makes it possible establish their relationship with the directions of the Umov–Poynting vector, and to investigate the spatial structure of the power fluxes. A description of either the scalar or vector fields individually has no such quality. Moreover, such a possibility is achieved using small vector-scalar receivers with dimensions much smaller than the wavelength and length of anomalous field zones in the vertical and horizontal planes. This allows a detailed study of the characteristics of these zones, including in the zone near the minima of the SP and VVV.

Good agreement was established between the interference dependences and extreme zones of maxima and minima obtained experimentally and numerically, but only when using models of the waveguide transfer function constructed from data on acoustic calibration of the waveguide and adequate estimates of the seafloor model parameters. It has been confirmed that smooth phase gradients are observed in the zones of maxima, which can be described analytically and approximated by the effective phase velocity. In zones of deep minima, poles form and jumps of up to 180° for the horizontal phase gradient and up to ±180° for the vertical phase gradient occur.

The spatial characteristics of the projections of the VVV and the phase gradient of the SP have been studied in detail, and their horizontal and vertical projections have been calculated. This made it possible to construct hodographs of the indicated values, which when analyzed yielded a conclusion on the formation of vorticity in the vertical plane: circulation in the zone of the pole (dislocations). In the horizontal plane, when the transfer functions are isotropic, there should be no acoustic vortices.

The directions of the phase gradient of the SP deviate from the horizontal only in the dislocation zone and vary in this zone within limits close to $\pm\pi$. The directions of the VVV substantially depend on the waveguide depth, since with varying depth, the relation between the horizontal and vertical VVV components changes. The modulus of the total VVV approaches zero in the zone of minimum pressure amplitude.

Analysis of the sound field characteristics in IMI zones is primarily of theoretical interest. From a practical viewpoint, it is more important to study the sound field characteristics in IMA zones, since it is here that one observes not only maximum signal-to-noise ratios, but also stable and predictable SP phase gradients and maximum values of the horizontal projection of the VVV. These factors make it possible, when arrays are located in IMA zones, to achieve unbiased estimates of the bearing and obtain the highest the axial concentration coefficients even at oblique wave angles of incidence. The Umov–Poynting vector in the IMA zones has a horizontal direction, which indicates horizontal propagation of sound energy in these zones. Using the special properties of IMA zones—the formation of "crests"—allows, taking into account the laws of the Chuprov energy invariant, effective detection, direction finding, and estimation of the distance to a moving source [18, 19]. Therefore, the authors believe that additional studies of the regularities of changes in the "surfaces" formed precisely by IMA zones, in particular, the dynamics of interference crests, are of great importance.

When solving such problems, interesting scientific results can be obtained using VSRs, which give significantly more information in the spatial domain than scalar receivers.

FUNDING

The study was supported by the program Shallow Water Acoustics, Nonlinear Acoustic Diagnostics, and Nonlinear Wave Dynamics (state registration no. AAAA-A18-118021390174-1) and the Russian Foundation for Basic Research (project no. 19-08-00941).

REFERENCES

1. V. A. Zhuravlev, I. K. Kobozev, and Yu. A. Kravtsov, Zh. Eksp. Teor. Fiz. **104** (5(11)), 3769 (1993).
2. V. A. Eliseevnin and Yu. I. Tuzhilkin, Acoust. Phys. **47** (6), 688 (2001).
3. V. M. Kuz'kin, A. V. Ogurtsov, and V. G. Petnikov, Acoust. Phys. **44** (1), 77 (1998).
4. G. N. Kuznetsov, O. V. Lebedev, and A. N. Stepanov, Acoust. Phys. **62** (6), 717 (2016).
5. N. I. Belova, G. N. Kuznetsov, and A. N. Stepanov, Acoust. Phys. **62** (3), 328 (2016).
6. V. A. Shchurov, Chin. J. Acoust. **38** (2), 113 (2019).
7. V. A. Shchurov, V. P. Kuleshov, and A. V. Cherkasov, Acoust. Phys. **57** (6), 851 (2011).

8. G. N. Kuznetsov, in *Proc. 17th School-Seminar Named after L. M. Brekhovskikh, Academician Jointed with 33rd Session of Russian Acoustical Society. Ocean Acoustics* (Shirshov Institute of Oceanology RAS, Moscow, 2020), p. 371 [in Russian].
9. A. I. Belov and G. N. Kuznetsov, Acoust. Phys. **59** (6), 674 (2013).
10. A. I. Belov and G. N. Kuznetsov, Acoust. Phys. **62** (2), 194 (2016).
11. A. I. Belov and G. N. Kuznetsov, Fundam. Prikl. Gidrofiz. **8** (1), 68 (2015).
12. G. N. Kuznetsov and A. N. Stepanov, Acoust. Phys. **59** (3), 333 (2013).
13. G. N. Kuznetsov and A. N. Stepanov, Acoust. Phys. **63** (6), 660 (2017).
14. G. N. Kuznetsov and O. V. Lebedev, Acoust. Phys. **58** (5), 575 (2012).
15. G. N. Kuznetsov and A. N. Stepanov, Acoust. Phys. **66** (4), 390 (2020). https://doi.org/10.1134/S1063771020040053
16. G. A. Grachev and G. N. Kuznetsov, Sov. Phys. Acoust. **31** (5), 408 (1985).
17. L. M. Brekhovskikh and Yu. P. Lysanov, *Theoretical Foundations of Ocean Acoustics* (Nauka, Moscow, 2007) [in Russian].
18. G. N. Kuznetsov, V. M. Kuz'kin, and S. A. Pereselkov, Gidroakustika, No. 34 (2), 26 (2018).
19. G. N. Kuznetsov, V. M. Kuz'kin, and S. A. Pereselkov, Acoust. Phys. **63** (4), 449 (2017).